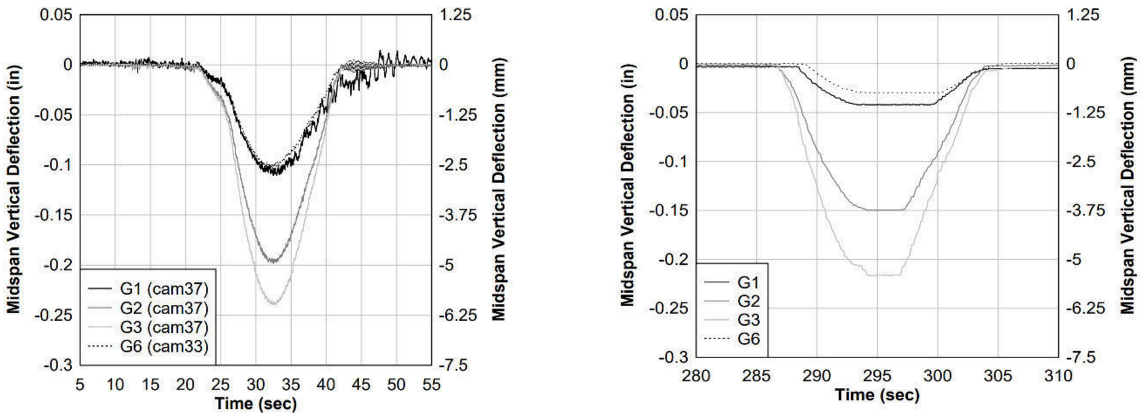

Fig. 5—Displacement time history at select girders 1, 2, 3 and 6 per Test 2 (tandem trucks) captured by (a) Imetrum DMS and (b) string potentiometers connected to underside of each girder.

Live load distribution factors (LLDFs) for each truck load per beam were calculated using the midspan displacements measurement from the strain transducers placed on the bottom flange of each girder at midspan and from the Imetrum system. Tables 3 and 4 show the results from the strain and displacement measurements along with the LLDFs computed per girder for the heavier loaded truck (Truck 1) and tandem trucks (Trucks 1 and 2). A single girder line analysis using BRASS-GIRDER was also performed for a DelDOT 2735 truck and resulted in a displacement of 3.9 mm (0.15 in.) compared to 3.3 mm (0.13 in.) of displacement obtained from the vision-based (displacement) measurement shown in Table 3.

Table 3—Live load distribution factors (LLDFs) for Test 1 (one-lane loaded) based on strain and displacements measurements.

Girder	1	2	3	4	5	6
Strain (με)	28	65	73	41	21	3
Displacement, mm (in.)	2.1 (0.08)	3.3 (0.13)	3.3 (0.13)	2.8 (0.11)	1.6 (0.06)	0.8 (0.03)
LLDF με	0.12	0.28	0.31	0.18	0.09	0.01
LLDF Δ	0.15	0.24	0.24	0.20	0.12	0.06

Table 4—Live load distribution factors (LLDFs) for Test 2 (tandem loading) based on strain and displacements measurements.

Girder	1	2	3	4	5	6
Strain (με)	36	93	123	121	81	34
Displacement, mm (in.)	2.8 (0.11)	5.1 (0.2)	6.1 (0.24)	6.1 (0.24)	5.1 (0.2)	2.8 (0.11)
LLDF με	0.15	0.38	0.51	0.50	0.33	0.14
LLDF Δ	0.2	0.36	0.44	0.44	0.36	0.19

Structural modeling

SAP2000 is utilized to create a bridge model for the finite element analyses. The bridge grillage model in SAP2000 consists of frame sections for the non-composite W36x210 rolled beam and the bridge deck were defined separately and connected by fully rigid linear link elements every 305 mm (1 ft) along the beam's 19.8-m (65-ft) span. Non-rigid link elements were used to link the deck nodes to their nearest girder, where the vertical displacement and in-plane moments were analyzed and compared to the data from the load test. Once the bridge model was generated, it was used to calibrate the model using the results from the load test. From the vision-based measurement data (Imetrum DMS), the lateral distribution of girder deflection from a truck passing over Lane 1, one girder received 25% of the superstructure's deflection. Applying 25% of the three axles from the DelDOT Truck 2735 load in SAP2000 resulted in displacements and strains within 5% difference of what was measured during the load test shown in Tables 5 and 6. Initially for Test 1, SAP2000 estimated the summation of midspan girder displacement, Δ = 7.4 mm (0.29 in.). To adjust the estimated displacement in the grillage model, frame properties stiffness modification factors were applied. Based on the strain measurements from strain gauges placed near the bridge bearings, it was discovered that the bearings provided significant restraint. Having a steel girder and concrete deck stiffness modification factor of 0.72 resulted in a displacement of 3.3 mm (0.13 in.) in Girder 3, 26% of the girder system's lateral distribution of live load deflection.

Hand calculations for the composite W36x210 rolled beam were performed and compared to the SAP2000 results. Live load distribution factors using the AASHTO LRFD Bridge Design Specifications (2020), Lever Rule Grillage Model, and Finite Element Model data for moment, deflection, and shear to evaluate the lateral distribution due to live load were compared. Based on the lateral distribution live load distribution factor for truck load per beam ($LLDF_{truck}$) and Operating Rating Factor (RF_{OPR}) were also calculated and compared. Tables 5 and 6 show a side-by-side comparison of the LLDF obtained from BRASS-GIRDER, load testing (measured field data), finite element modeling using SAP2000 for one-lane (single lane) and multiple lanes (M-lanes), and AASHTO LRFD Bridge Design Specifications (2020) approximations for the live load distribution using various measurements and methods.

Table 5—Comparison of LLDFs based on live load distribution from deflection measurements.

Deflection					
BRASS-GIRDER (mg)		Field Test (mg)		SAP2000 (mg)	
1-lane	M-lanes	1-lane	M-lanes	1-lane	M-lanes
0.2	0.43	0.3	0.44	0.39	0.49

Table 6—Comparison of LLDFs for moment computed using various methods.

Moment							
AASHTO (mg)		BRASS-GIRDER (mg)		Field Test (mg)		SAP2000 (mg)	
1-lane	M-lanes	1-lane	M-lanes	1-lane	M-lanes	1-lane	M-lanes
0.48	0.67	0.52	0.72	0.38	0.51	0.39	0.49

Based on the lateral distribution live load distribution factor for the truck load per beam ($LLDF_{truck}$), an Operating Rating Factor (RF_{OPR}) was calculated using the strain measurements (Table 6), and if the distributions from displacements were used instead of strain measurements. Operating Rating Factors (RF_{OPR}) calculations were completed based on data from this diagnostic load test (TRB 2019) to compare if displacement measurements could be used instead of strains to perform load ratings in a non-contact, efficient yet accurate way.

Table 6—Operating rating factors for strain measurements at midspan from mounted strain transducers and vision-based displacement measurements at midspan using the Imetrum DMS (non-contact).

Strain Measurements		Vision-based Measurements	
W_r	70 kips (311 kN)	W_r	70 kips (311 kN)
W_p	62.95 kips (280 kN)	W_p	62.95 kips (280 kN)
γ_{LL}	1.3	γ_{LL}	1.3
I	1.29	I	1.29
f_v	0.99	f_v	0.99
tandem RF_{opr}	1.49	tandem RF_{opr}	1.49
max. $\mu\varepsilon$ single truck	83.24	max. Δ single truck	0.13
max. $\mu\varepsilon$ tandem truck	123.44	max. Δ tandem truck	0.24
measured tandem/single ratio*	1.48	measured tandem/single ratio*	1.78
single RF_{opr}	2.21	single RF_{opr}	2.66

*1.67 was the expected value

CONCLUSIONS

The results from this study showed how live load distribution factors obtained from strain measurements compared favorably to the distributions obtained from vision-based displacement measurements during a diagnostic load test. The use of computer vision and other vision-based measurements offer many options for conducting load tests and obtaining the necessary data without having direct contact on the bridge via mounted sensor arrays. The results from this study revealed the sensitivity and accuracy of the displacement measurement when compared to conventional string potentiometer readings when mounted directly to the flange of the girder. While there is not one optimal technique for measuring structural displacements based on a video, different techniques have different performance levels, and the applicability of these various methods may vary from case to case. The goal of this paper was to compare the performance and accuracy of vision-based displacement measurements in form of a field experiment on a bridge, and how the data can be used to calibrate finite element models that can be used to inform load ratings.

SUMMARY AND CONCLUDING REMARKS

Given the many bridges in the United States that are near the end of their design life span, advanced technologies like vision-based measurements provide an alternative towards understanding the existing load-carrying capacity of a bridge in a non-contact way. The primary goal of the live load testing was to confirm that the distribution factors per AASHTO LRFD Bridge Design Specifications (2020) revealed to be conservative when compared to measured data obtained from non-contact vision-based measurements that were used to calibrate a finite element model. Based on the findings, a procedure to evaluate live load distribution to inform load ratings may be possible based on the distribution of displacements using vision-based measurements that are simpler and require less time and resources to complete while being accurate and reliable. However, more research is needed to validate that displacement data obtained from non-contact, vision-based methods can be used to calibrate finite element models, which, in turn, can be used to better approximate live load distributions and therefore perform a load rating using the AASHTO LRFR rating factors.

ACKNOWLEDGEMENTS

Funding for this study was provided by the U.S. Department of Transportation (USDOT) Region 3 University Transportation Center, *The Center for Integrated Asset Management for Multimodal Transportation Infrastructure Systems* (CIAMTIS). The authors express gratitude to the Delaware Department of Transportation (DelDOT) for their guidance to support the load test. Any opinions, findings, conclusions, recommendations presented in this paper are those of the authors and do not necessarily reflect those of the funding agencies, Bridge Diagnostics Inc., Imetrum or DelDOT.

REFERENCES

American Association of State Highway and Transportation Officials (AASHTO) (2020). *AASHTO LRFD Bridge Design Specifications*, 9th Edition, Washington, DC.

American Association of State Highway and Transportation Officials (AASHTO) (2018). *Manual for Bridge Evaluation, 3rd edition, 2018 interim revisions.* American Association of State Highway and Transportation Officials, Washington, DC.

Alipour, M., Washlesky, S. J., & Harris, D. K. (2019). Field Deployment and Laboratory Evaluation of 2D Digital Image Correlation for Deflection Sensing in Complex Environments. *Journal of Bridge Engineering*, *24*(4), 1–15. https://doi.org/10.1061/(ASCE)BE.1943-5592.0001363.

Al-Khateeb, H., Shenton, H.W. III, Chajes, M.J. (2018). Computing continuous load rating factors for bridges using structural health monitoring data. *Journal of Civil Structural Health Monitoring,* 8:721-735.

Betti, R.M., Sloane, M.J., Khazem, D., Gatti, C. (2016). Monitoring the structural health of main cables of suspension bridges. *Journal of Civil Structural Health Monitoring,* 6:355-363.

Brownjohn, J.M., Kripakaran, W.P., Harvey, B., Kromanis, R., Jones, P., Huseynov, F. (2016). Structural health monitoring of short to medium span bridges in the United Kingdom, *Structural Monitoring Maintenance,* 3:259-276.

Chen, J.G., Wadhwa, N., Cha, Y.-J., Durand, F., Freeman, W.T., and Buyukozturk, O. (2015). "Modal identification of simple structures with high-speed video using motion magnification." *Journal of Sound and Vibration,* 345, 58-71.

Das, S. and Saha, P. (2018). "A review of some advanced sensors used for health diagnosis of civil engineering structures." *Measurement,* 129, 68-90.

Doebling, S.W., Farrar, C.R., Prime, M.B., Shevitz, D.W. (1996). Damage identification and health monitoring of structural and mechanical systems from changes in the vibration characteristics: a literature review. Los Alamos National Laboratory, New Mexico.

Eom, J. and Nowak, A.S. (2001). "Live Load Distribution for Steel Girder Bridges." Journal of Bridge Engineering, Vol. 6, No. 6, November/December, pp 489-497.

Farrar, CR, Darling TW, Migliori A, Baker WE (1999). Microwave interferometers for non-contact vibration measurements on large structures. Mech Syst Signal Process 1999; 13:241-53.

Harris, D. (2010). Assessment of flexural lateral load distribution methodologies for stringer bridges. *Engineering Structures, 32*(11), 3443-3451. http://doi.org/10.1016/j.engstruct.2010.06.008
Retrieved from: https://digitalcommons.mtu.edu/michigantech-p/6351.

Imetrum. (n.d.) VideoGauge™ - how it works. Last accessed on February 1, 2022 from http://www.imetrum.com/video-gauge/how-it-works.

Kim, Y.J., Murison, E., Mufti, A. (2010). Structural health monitoring: a Canadian perspective. *Proc Inst Civ Eng-Civ Eng,*163:185-191.

Kim, S. and Nowak, A.S. (1997). "Load Distribution and Impact Factors for I-Girder Bridges." Journal of Bridge Engineering, Vol. 2, No. 3, August, pp 97-104.

National Bridge Inventory (NBI) (2021). Last accessed on February 1, 2022 from <https://www.fhwa.dot.gov/bridge/nbi.cfm>.

NYSDOT (2007). *Reliability of visual inspection for highway bridges.* NYSDOT Engineering Division Office of Structures, Albany, NY.

Seo, J., Phares, B., Lu, P., Wipf, T., Dahlberg, J. (2013). Bridge rating protocol using ambient trucks through structural health monitoring system. *Engineering Structures,* 46:569-580.

Seo, Junwon & Duque, Luis & Wacker, Jim. (2018). Drone-enabled bridge inspection methodology and application. Automation in Construction. 94. 112-126. 10.1016/j.autcon.2018.06.006.

Shenton, H.W. III, Al-Khateeb, H.T., Chajes, M.J., Wenczel, G. (2017). Indian River Inlet Bridge (Part A): description of the bridge and the structural health monitoring system. *Bridge Structures* 13(1): 3-13.

Stanbridge, Anthony B., Milena Martarelli, David J. Ewins (2000), "Measuring area vibration mode shapes with a continuous-scan LDV," Proc. SPIE 4072, Fourth International Conference on Vibration Measurements by Laser Techniques: Advances and Applications, (22 May 2000); https://doi.org/10.1117/12.386746.

Sohn, H., Farrar, C. R., Hemez, F., & Czarnecki, J. (2001). A Review of structural health. *Library.Lanl.Gov*, 1–7. https://library.lanl.gov/cgi-bin/getfile?00796820.pdf

Sony, S., Laventure, S., and Sadhu, A. (2019). "A literature review of next-generation smart sensing technology in structural health monitoring." *Structural Control and Health Monitoring,* 26(3), e2321_eprint: https://onlinelibrary.wiley.com/doi/pdf/10.1002/stc.2321.

Sun, Limin, Shang, Zhiqiang, Xia, Ye, Bhowmick, Sutanu, and Nagarajaiah, Satish (2020). "Review of Bridge Structural Health Monitoring Aided by Big Data and Artificial Intelligence: From Condition Assessment to Damage Detection." *Journal of Structural Engineering,* 2020, 146(5): 04020073.

Transportation Research Board (TRB) (2019). *Primer on Bridge Load Testing.* Transportation Research Circular, Number E-C257, November 2019.

Xu, Y. and Brownjohn, J.M.W. (2018). "Review of machine-vision based methodologies for displacement measurement in civil structures." *Journal of Civil Structural Health Monitoring,* 8(1), 91-110.

Zokaie, T. (2000). "AASHTO-LRFD Live Load Distribution Specifications." Journal of Bridge Engineering, Vol. 5, No. 2, May, pp 131-138.

ACI Member **Monique H. Head**, PhD, is an Associate Professor and Associate Chair in the Department of Civil and Environmental Engineering at the University of Delaware. She is a voting member of ACI Committee 440H (FRP Reinforced Concrete) and 341 (Earthquake-Resistant Concrete Bridges). Her interests include bridge engineering, load testing, and performance-based seismic design.

ACI student member **Luke Timber** is a graduate student in the Department of Civil and Environmental Engineering at the University of Delaware. He is a student member of ACI. His research interests include bridge engineering and load testing using digital image measurements.

Effects of Barriers on Load Distribution in a Concrete Slab-Span Bridge

Kendall A. Hill, Benjamin Z. Dymond, Brock D. Hedegaard, Lauren E. Linderman

Synopsis: Characterization of load distribution is useful for determining the load rating of bridges, and results in the literature have shown that the structure type and presence of secondary elements both impact this distribution. The focus of this study was to determine how the load distribution in a concrete slab-span bridge was affected by the presence of concrete barriers through finite element modeling and a truck live load test. There are minimal studies reported in the literature that quantify this phenomenon in slab-span bridges. A three-dimensional solid-element finite element model was used to determine the distribution when load was placed near and away from a barrier. Truck testing utilized strain gauges and displacement transducers to characterize the effects of a barrier on load distribution. Results indicated that the barrier had an impact on load distribution in concrete slab-span bridges. This impact could be quantified to determine the live load demand more accurately for use in load rating a concrete slab-span bridge.

Keywords: barrier, bridge, finite element model, instrumentation, load distribution, load rating, reinforced concrete, slab-span, truck test

RESEARCH OBJECTIVE

The objective of this research was to determine if the presence of barriers on slab-span bridges affects the load distribution and if the effect is quantifiable. Both finite element modeling and field testing of a reinforced concrete slab-span bridge were used to evaluate the impact of barriers. The solid-element model used the bridge dimensions from the as-built plans and in-situ material properties. Load was placed near and away from the barrier; the barrier behavior was bounded by considering both a fully rigid connection between the slab and barrier and excluding the barrier from the model. A field-based truck test was also conducted to quantify the load distribution during live load testing via data from strain gauges and linear variable displacement transducers (LVDTs). The field test data were used to identify which modeling technique behaved most similarly to the structure under evaluation.

RESEARCH SIGNIFICANCE

This project is motivated by the growing need to evaluate bridges and structures that have reached their design life without scheduled replacement or improvement. Numerical design and evaluation methods may result in poor load ratings for older structures, which may funnel traffic, especially oversize-overweight vehicles, onto secondary roads. Load ratings have been improved through field testing and finite element analysis; barriers and other secondary elements have been identified as carrying portions of the load. This study quantified the improvement in load distribution that may be attributed to concrete barriers in slab-span bridges.

BACKGROUND

Slab-span bridges are typically flat slabs of reinforced concrete cast in falsework formwork over piers and abutments. They may have one or more spans ranging from 20 to 50 ft (6.1 to 15.2 m). These structures have historically been one of the most economic solutions for short, simple, and continuous span structures (Conkel 2019). Slab-span bridges do not have girders, which allows for a thinner structure. This facilitates the construction of curved structures and superelevated structures. The structure thickness is typically between 15 and 24 in. (38 and 61 cm), which allows for the placement of two layers of transverse and longitudinal reinforcement to resist negative and positive flexure. The aspect ratio of the slab (span length-to-thickness) is typically between 16 and 30.

Load rating of slab-span bridges is governed by the American Association of State Highway and Transportation Officials (AASHTO). Load ratings are obtained through calculations or live load testing of a structure. The AASHTO Manual for Bridge Evaluation (MBE) (2018) sets guidelines for load rating bridges. The load rating is expressed either as a rating factor (RF) or a vehicle weight. The following equations present the general expression for determining the load rating of a structure, which can be used in either load factor rating (LFR) (Eq. (1)) or load and resistance factor rating (LRFR) (Eq. (2)) methods.

$$\mathrm{RF} = \frac{C_M - A_1 D}{A_2 L(1+IM)} \tag{1}$$

$$\mathrm{RF} = \frac{C_S - \gamma_{DC} DC - \gamma_{DW} DW \pm \gamma_P P}{\gamma_L LL(1+IM)} \tag{2}$$

where RF is the rating factor; C_M is the member capacity; D is the dead load effects on the member; A_1 is the factor for the dead loads; A_2 is the factor for the live loads; L is the live load effects on the member; IM is the dynamic load allowance used with the live load effect; C_S is the structural capacity; DC is the dead-load effect of structural components and attachments; DW is the dead-load effect of wearing surfaces and utilities; P is the permanent loading other than dead loads; LL is the live-load effect; γ_{DC} is the load factor for structural components and attachments; γ_{DW} is the load factor for wearing surfaces and utilities; γ_P is the load factor for permanent loads other than dead loads; and γ_L is the evaluation live-load factor (AASHTO 2018). Load effects can be axial force, vertical shear force, bending moment, axial stress, shear stress, and bending stresses (AASHTO 2018).

The live load demand used in the LRFR methodology consists of the AASHTO HL-93 design load from the AASHTO LRFD Specifications (2020), which includes both the HS-20 truck and a distributed lane load; the live load demand used in the LFR method includes either the HS-20 truck load or the distributed lane load from the AASHTO Standard Specifications (2002). Once the load effect being evaluated is selected, the capacity of the structure is also determined. To compute the member rating in the LFR method, the rating factor is multiplied by the weight of the truck used to determine the live load effects (AASHTO 2018). The bridge rating should be checked for each member and the overall bridge rating is often controlled by the member with the lowest rating factor.

Load distribution is a key component of the demand calculation when load rating a slab-span bridge. Rather than determining the load carried by a girder, the portion of load carried by a width of slab is needed. The live load in Eq. (1) and Eq. (2) is obtained by multiplying the code-based demand by the live load distribution factor (LLDF) shown in Eq. (3). The LLDF for slab-span bridges is taken as the inverse of the equivalent width E in inches divided by 12 in. per ft.

$$\text{LLDF} = {}^{12}/_{E} \tag{3}$$

The AASHTO LRFD (2020) equivalent strip width equations for a single lane or multiple lanes loaded are presented in Eq. (4) and (5), respectively. The equivalent strip width equation for exterior strips (carrying one wheel path) is shown as Eq. (6) (2017). Equivalent width values calculated using the AASHTO Standard Specifications (2002) for a single wheel path can be obtained from Eq. (7), which results in a width in ft that may be applied to the load distribution factor without the unit conversion in Eq. (3).

$$E = 10 + 5\sqrt{L_1 W_1} \tag{4}$$

$$E = 84 + 1.44\sqrt{L_1 W_1} \leq 12\frac{W}{N_L} \tag{5}$$

$$E = D + 12 + \frac{E_{min}}{4} \tag{6}$$

$$b_{eff} = 4 + 0.06S \tag{7}$$

Where E is the equivalent width (in.), L_1 is the span length (ft) less than or equal to 60 ft; W_1 is the bridge width (ft) less than or equal to 30 ft for single lane loading and 60 ft for multilane loading; W is the actual bridge width (ft); N_L is the number of lanes taken as the road width divided by 12 ft/lane; D is the distance from edge to inside of barrier (in.); E_{min} is the minimum value obtained from Eq. (4) or (5) (in.); b_{eff} is the distribution width for one wheel path (ft); and S is the span length (ft).

The equations used for determining the equivalent width, as well as load ratings, for slab-span bridges have been shown to be conservative in the literature (Azizinamini et al., 1994b, 1994a; Azizinamini & Choobineh, 1995; Csagoly & Lybas, 1989; Freeman & Vasconcelos, 2018; Jones et al., 2012; Mabsout et al., 2004). A study by Freeman and Vasconcelos (2018) compared load ratings of bridges in the Florida DOT inventory using the LFR method to a different structural analysis for load distribution (SALOD) method, which decreased the distribution factor of bridges rated by the LFR method by 11% and increased the load rating by 13%. The SALOD method uses a database of interaction surfaces found using the finite element method (Hays et al., 1986). In addition, a study by Jones et al. (2012) found that using strain data obtained from truck tests resulted in equivalent widths for single lane and multilane loaded cases that were 116% and 33% greater than AASHTO LRFD (1994) values, respectively.

Freeman and Vasconcelos (2018) presented the section modulus method shown in Eq. (8) for determining the equivalent width using strain data from field data or FEM results.

$$E = \frac{\sum w_i \varepsilon_i s_i}{\varepsilon_n s_n} \tag{8}$$

where E is the effective width (in.), w_i is the width of the section for the section modulus method (in.), ε_i is the strain at section i for the section modulus method (in./in.), S_i is the section modulus for the width where the strain was obtained (in.^{3}), ε_n is the strain at the point of interest (in./in.), and S_n is the section modulus at the point of interest (in.^{3}).

Jones et al. (2012) presented an “area under the curve” method shown in Eq. (9) for determining the equivalent width from field or FEM strain data taken across midspan of the structure.

$$E = \frac{A_\varepsilon - A_t}{\varepsilon_{max}} + w_t \tag{9}$$

where A_ε is the area under the strain curve (in.), A_t is the area under the strain curve between the truck wheel patches (in.), ε_{max} is the maximum measured strain (in./in.), and w_t is the width of the truck (in.).

The section modulus method uses each strain value from each location that strain is measured across the width of the slab, which can be more accurate than taking the largest observed strain. The section modulus method also considers added stiffness from curbs or barriers that are not accounted for by AASHTO design or evaluation equations. While the load rating equations have been shown to be conservative, live load testing can clarify and reduce uncertainty related to the structural performance of a bridge (Sherman et al., 2020).

FINITE ELEMENT MODELING METHODOLOGY

A solid-element finite element model of a slab-span bridge from the Minnesota Department of Transportation (MnDOT) inventory (Bridge 27926) was developed using the static structural analysis package in ANSYS. A three-dimensional modeling technique was selected rather than a shell element model to include observed cracking in the structure as well as the measured material properties of the steel reinforcement. The model was developed using the bridge geometry shown in Fig. 1 and Fig. 2. The structure has three continuous spans with end spans of 23 ft 7 in. (7.2 m) and a middle span of 24 ft 2 in. (7.4 m). The slab thickness was 11 in. (28 cm). The outside edge-to-outside edge width of the slab was 44 ft 9 in. (13.6 m). One elastic model and two inelastic models with steel reinforcement and simulated cracking were created to provide upper and lower bounds of possible bridge behavior:

1) Elastic Model – In-situ elastic material properties.
2) Inelastic Model with 2-in. (5-cm) cracks – In-situ elastic and inelastic material properties with four simulated 2-in. wide by 6-in. deep (5-cm by 15-cm) cracks on the bottom of the slab.
3) Inelastic Model with 24-in. (61-cm) cracks – In-situ elastic and inelastic material properties with seven simulated 24-in. wide by 6 in. deep (61-cm by 15-cm) cracks on the bottom of the slab.

Mean measured in-situ material properties shown in Table 1 were obtained by testing specimens that were collected while coring the bridge slab as shown in Fig. 3. All material property specimen testing was completed in accordance with appropriate ASTM International standards.

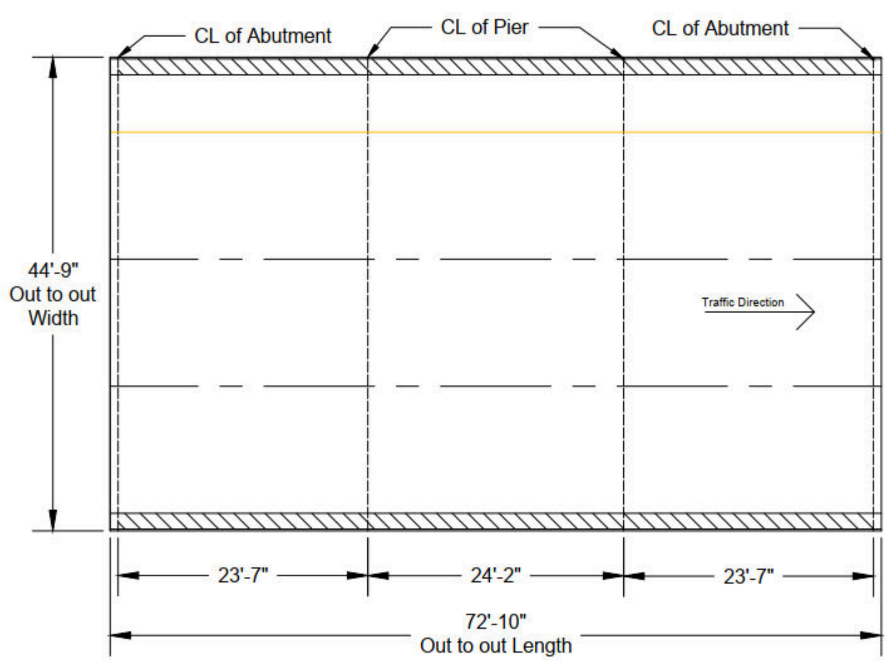

Fig. 1—Plan view of the slab-span bridge. [1 ft = 30 cm and 1 in. = 2.54 cm]

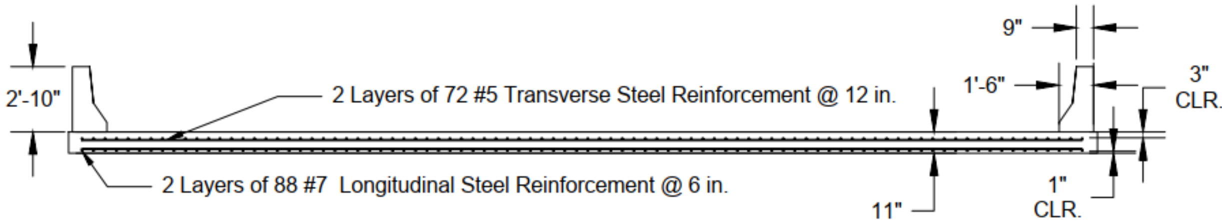

Fig. 2—Cross-sectional view of the slab-span bridge. [1 ft = 30 cm and 1 in. = 2.54 cm]

Fig. 3—Coring rig used to obtain material samples from the slab-span bridge.

Table 1—Measured material properties from the slab-span bridge.

Member	Compressive Strength, f'_c psi (MPa)	Modulus of Elasticity, E ksi (GPa)	Yield Strength, f_y psi (MPa)
Concrete Slab	9480 (65.4)	3730 (25.7)	—
Concrete Barrier	11025 (76.0)	—	—
#7 Steel Reinforcement	—	29800 (205.5)	80400 (554.3)

The elastic FEM model used the elastic concrete isotropic elasticity properties, including modulus of elasticity obtained from in-situ material samples and an estimated Poisson's ratio of 0.2 (AASHTO, 2020). The reinforcement bars were not accounted for in the elastic model. The concrete barriers were either modeled as fully connected via a surface-to-surface bond to the concrete slab or suppressed from the model to obtain results without barriers. The connections at the abutments and piers were fixed, except rotation in the direction of traffic was allowed.

The inelastic model was created using the same isotropic elasticity properties as the elastic model with the addition of Menetrey-Willam properties for nonlinear concrete material behavior, including uniaxial compressive (9480 psi or 65.4 MPa), biaxial compressive (10430 psi or 71.9 MPa), and tensile (320 psi or 2.2 MPa) strengths. The steel reinforcement was modeled and bonded to the surrounding concrete. The steel isotropic elasticity and isotropic multilinear hardening were modeled using yield and post yield data from field-sampled steel reinforcing as shown in Fig. 4. These inelastic models were created to characterize the effects of longitudinal cracking on the underside of the concrete slab shown in Fig. 5. These models split the underside of the slab into longitudinal strips that either retained the measured value for the modulus of elasticity or strips with a modulus of elasticity value near zero. The first inelastic model had four strips that were 2-in. (5-cm) wide, extended 6 in. (15 cm) up into the slab thickness, and were evenly spaced transversely across the bridge width consistent with crack spacing observed in the field. The second inelastic model had seven strips that were 24-in. (61-cm) wide, extended 6 in. (15 cm) up into the slab thickness, and were evenly spaced transversely across the bridge width consistent with crack spacing observed in the field. The crack depth of 6 in. (15 cm) was selected because it is approximately the distance from the bottom of the slab to the lowest fiber